Carbon Energy

WILEY

CARBON ENERGY

RESEARCH ARTICLE OPEN ACCESS

Transformative Catalytic Carbon Conversion Enabling Superior Graphitization and Nanopore Engineering in Hard Carbon Anodes for Sodium-Ion Batteries

Guilai Zhang[1] | Hong Gao[1,2] | Dingyi Zhang[1] | Jun Xiao[1] | Limeng Sun[1] | Jiayi Li[1] | Congcong Li[1] | Yiwen Sun[1] | Xinyao Yuan[1] | Peng Huang[3] | Yi Xu[1] | Xin Guo[4] | Yufei Zhao[5] | Yong Wang[1] | Yao Xiao[6] | Guoxiu Wang[5] | Hao Liu[5]

[1]Joint International Laboratory on Environmental and Energy Frontier Materials, School of Environmental and Chemical Engineering, Shanghai University, Shanghai, China | [2]State Key Laboratory of Advanced Special Steel, Shanghai Key Laboratory of Advanced Ferrometallurgy, Shanghai University, Shanghai, China | [3]School of Chemistry and Materials Science, Jiangsu Normal University, Xuzhou, Jiangsu, China | [4]Faculty of Materials Science and Energy Engineering, Shenzhen University of Advanced Technology, Shenzhen, Guangdong, China | [5]Centre for Clean Energy Technology, University of Technology Sydney, Broadway, Sydney, New South Wales, Australia | [6]College of Chemistry and Materials Engineering, Wenzhou University, Wenzhou, China

Correspondence: Hong Gao (hgao1122@shu.edu.cn); Yi Xu (Tree2000xy@shu.edu.cn); Peng Huang (huangpeng@jsnu.edu.cn); Guoxiu Wang (Guoxiu.Wang@uts.edu.au); Hao Liu (hao.liu@uts.edu.au)

Received: 29 October 2024 | **Revised:** 29 November 2024 | **Accepted:** 11 December 2024

Funding: This Study was supported by the National Natural Science Foundation of China (22209103), Science and Technology Commission of Shanghai Municipality (22010500400), and Australian Research Council (FT180100705).

Keywords: catalytic carbonization | graphitization | hard carbon | nanopores | sodium-ion batteries

ABSTRACT

Hard carbons are promising anode materials for sodium-ion batteries (SIBs), but they face challenges in balancing rate capability, specific capacity, and initial Coulombic efficiency (ICE). Direct pyrolysis of the precursor often fails to create a suitable structure for sodium-ion storage. Molecular-level control of graphitization with open channels for Na^+ ions is crucial for high-performance hard carbon, whereas closed pores play a key role in improving the low-voltage (< 0.1 V) plateau capacity of hard carbon anodes for SIBs. However, creation of these closed pores presents significant challenges. This work proposes a zinc gluconate-assisted catalytic carbonization strategy to regulate graphitization and create numerous nanopores simultaneously. As the temperature increases, trace amounts of zinc remain as single atoms in the hard carbon, featuring a uniform coordination structure. This mitigates the risk of electrochemically irreversible sites and enhances sodium-ion transport rates. The resulting hard carbon shows an excellent reversible capacity of 348.5 mAh g^{-1} at 30 mA g^{-1} and a high ICE of 92.84%. Furthermore, a sodium storage mechanism involving "adsorption–intercalation–pore filling" is elucidated, providing insights into the pore structure and dynamic pore-filling process.

1 | Introduction

Hard carbon (HC), endowed with abundant raw resources, is a non-graphitized carbon material distinguished by graphite microcrystals, turbulent layers, and nanopores. Within sodium-ion battery systems [1, 2], the HC anode shows prolonged and reversible charge/discharge plateaus at low potentials (lower than 0.1 V), reminiscent of the electrochemical characteristics observed in graphite anodes within lithium-ion battery systems [1–5]. This suggests that HC is a promising anode material for commercial sodium-ion batteries [6–9], and compared with alloy-based materials, titanium-based materials, and so forth,

Guilai Zhang, Hong Gao, and Dingyi Zhang contributed equally to this study.

HC materials have outstanding economic advantages due to high technological maturity and abundant resources [10–12].

Researchers have extensively explored diverse HCs derived from various precursors and synthesis conditions. Nevertheless, HC with plentiful defects and sodium-ion-irreversible pores presents challenges, including low initial Coulombic efficiency, sluggish sodium storage kinetics, and unstable cycling performance [13, 14]. Varying carbonization temperatures during HC synthesis can minimize defects and promote the formation of larger graphite-like domains, which aids in the insertion of sodium ions into interlayers and boosts plateau capacity [15, 16]. However, excessively high temperatures shrink the interlayer spacing, hindering sodium-ion intercalation. When heated to 2000°C, the plateau capacity becomes undetectable [17]. In addition to optimal layer spacing, the presence of closed nanopores is crucial for storing sodium [18, 19]. Recent persuasive studies have highlighted that closed pore structures provide excellent plateau capacity [20, 21]. However, creation of these closed pores presents significant challenges. Conventional methods often struggle with controlling pore size and distribution, and maintaining structural integrity during carbonization. For instance, Wang et al. adopted a high-temperature carbonization pathway following KOH chemical activation of anthracite, which initially produced open-pore disordered carbon [22]. These were later converted into closed pores within short-range carbon structures, achieving a capacity of 308.4 mAh g^{-1}, primarily contributed by the low-voltage platform. Zheng et al. developed a CO_2-etching and carbonization strategy that induced numerous closed nanopores [23]. This technique enhanced both the size and the storage capacity of the closed pores, while preserving the microsphere shape, resulting in a plateau capacity of 351.1 mAh g^{-1}.

Herein, we utilize zinc gluconate (ZG)-assisted carbonization of low-cost lotus seed shell waste to fabricate HC anodes for SIBs. Without multiple steps or harsh conditions, the HCs are prepared using a facile one-step pyrolysis process, which significantly reduces defects and introduces nanopores. This straightforward strategy enables the transformation of ZG into zinc oxide and its eventual volatilization at elevated temperatures to create extensive nanopores and etched carbon microcrystals. The resulting microstructure features curved, long-layered graphene with well-distributed nanopores and optimal layer spacing. Moreover, the persistence of trace zinc atoms as single atoms within the HC matrix enhances sodium-ion transport and recombination rates. These isolated metal atoms function similarly to non-metallic heteroatoms, providing a uniform coordination structure that minimizes the formation of electrochemically irreversible sites. The constructed carbon anode shows a remarkable reversible capacity of 348.5 mAh g^{-1} with an excellent initial Coulombic efficiency (ICE) of 92.84%, along with excellent cycling stability (90.05% capacity retention after 500 cycles) and outstanding rate capability (218.0 mAh g^{-1} at 500 mA g^{-1}), making it a commercially viable solution.

2 | Result and Discussion

In this research endeavor, advanced HC anodes are developed utilizing cost-effective lotus seed shells as the primary material. The precursor is milled with ZG to establish essential cross-links with zinc ions, which catalytically integrate short-range graphite fragments into extensive, low-defect graphitic layers during pyrolysis (Supporting Information S1: Figure S1). Carbonization is conducted at three different temperatures (1200°C, 1400°C, and 1600°C), resulting in three samples denoted as HC-1200, HC-1400, and HC-1600 (Figure 1A). Scanning electron microscopy (SEM) and transmission electron microscopy (TEM) analyses show that all samples have a blocky structure with abundant channels, both on the surface and internally (Supporting Information S1: Figure S2). However, the carbonization temperatures strongly influenced the microstructures. Specifically, as depicted in Figure 1B, the high-resolution TEM (HRTEM) image of HC-1200 displays a short-range disordered lattice. In contrast, HC-1400 shows long-range curved graphene layers that contain a significant number of nanopores; these structural features enhance the effective transportation and retention of Na^+ (Figure 1C). On increasing the temperature to 1600°C, further graphitization occurs, resulting in the formation of thicker carbon layers. This narrowing of the interlayer spacing subsequently hinders the intercalation of Na^+ ions (Figure 1D). The selected area electron diffraction (SAED) patterns provide confirmation of the structural changes that have occurred, with HC-1200 showing enhanced disorder and HC-1600 indicating increased graphitization (Supporting Information S1: Figure S3) [24–26]. This result indicates that as the carbonization temperature increases, pore size also increases due to the merging of micropores into mesopores, and the degree of microstructure ordering and graphitization also improves, albeit at the cost of reduced interlayer spacing. This study highlights the balance required between graphitization and interlayer spacing to optimize Na^+ ion storage and transport in HC anodes.

X-ray diffraction (XRD) and Raman tests are utilized to analyze and compare the microstructural differences among the various samples. XRD patterns (Figure 1E) clearly distinguish the crystallographic properties of HC-1200, HC-1400, and HC-1600. All three samples inherit peaks at approximately 23° and 43°, which can be attributed to the characteristic (002) and (100) crystal planes, respectively, of disordered graphite domains [27]. As the carbonization temperature increases, the (002) peak undergoes a shift toward a higher angle, accompanied by a notable sharpening effect, indicating more ordered graphitic microcrystals, enhanced crystallization, and reduced interlayer spacing. According to HRTEM analysis, the layer spacings of HC-1200, HC-1400, and HC-1600 are 0.44 nm, 0.38 nm, and 0.35 nm, respectively, showing excellent agreement with the XRD results. Typically, a reduction in defects and an elevation in the level of graphitization occur. This, in turn, results in a lower intensity ratio of the D-band to the G-band (I_D/I_G) in Raman analysis [28]. Surprisingly, contrary to expectations, the I_D/I_G ratio increases from 0.93 to 1.27 as the pyrolysis temperature increases (Figure 1F). This anomaly may be ascribed to the presence of abundant closed pores in HC-1600, which contribute to the disorder [29]. Furthermore, elemental mapping (Supporting Information S1: Figure S4) unveils the uniform dispersion of C, N, and O in the HC-1400 sample. Fourier transform infrared spectroscopy (FTIR) further confirmed the C═O and C–N sites (Figure 1G) [30]. This shows that ZG-assisted carbonization not only retains nonmetallic elements from the native material but also facilitates sodium-ion storage capability through the adsorption of sodium by the detected

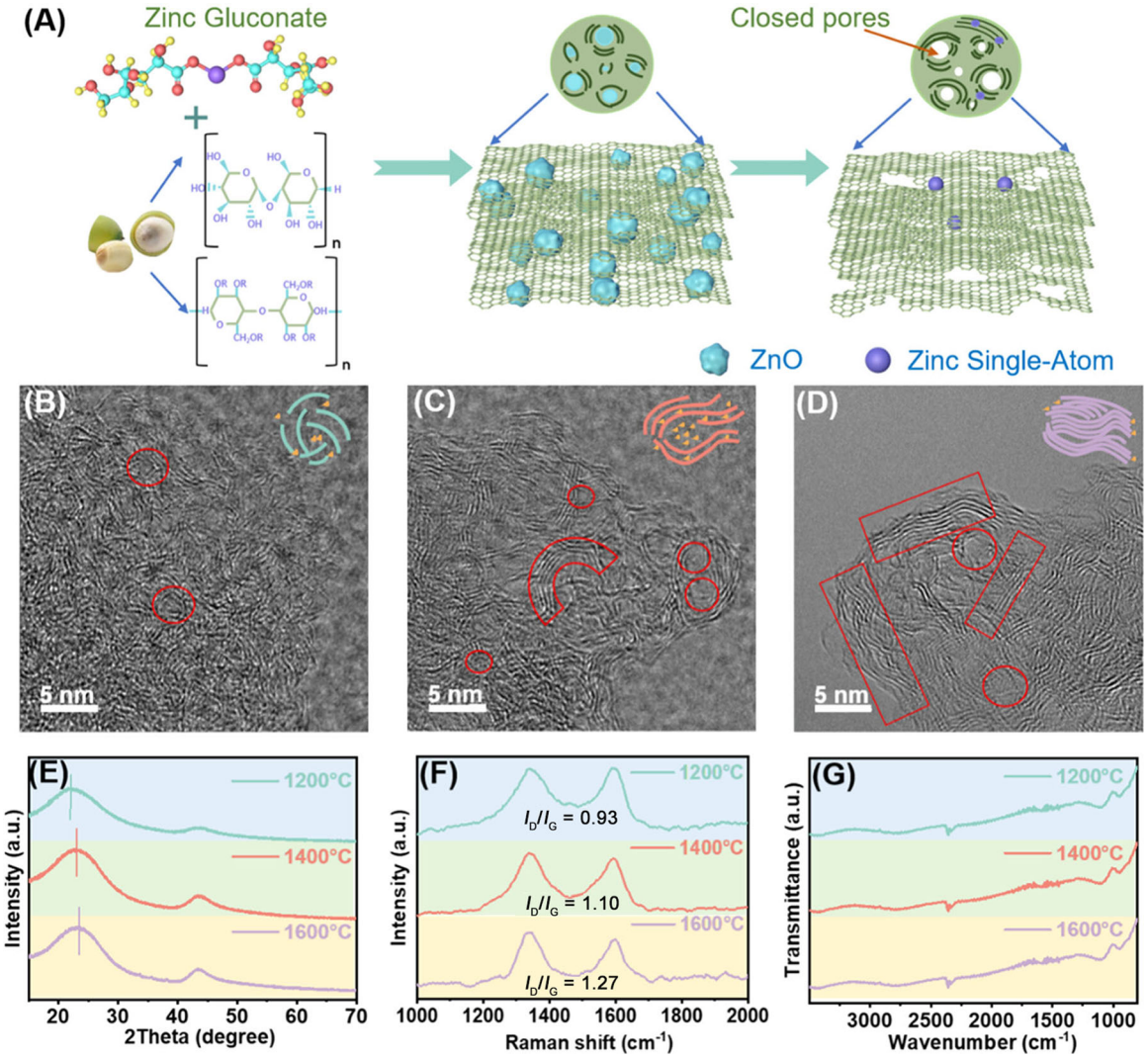

FIGURE 1 | (A) Schematic illustration of the preparation process of HC. HRTEM images and structural illustrations of HC regulated by different temperatures of (B) HC-1200, (C) HC-1400, and (D) HC-1600. (E) XRD patterns, (F) Raman spectra, and (G) FTIR of as-prepared HC anodes.

functional groups. Overall, these findings indicate that higher carbonization temperatures lead to increased graphitization and closed pore formation, which can influence the material's disorder and sodium storage properties.

To examine the effect of the carbonization process on the phase composition of HC and ZG mixtures, we analyzed the structural evolution and nanopore formation at various temperatures of 100, 200, 400, 600, 800, and 1000°C (denoted as ZG/HC-200, ZG/HC-400, ZG/HC-600, ZG/HC-800, and ZG/HC-1000, respectively). The XRD patterns of the pristine HC and ZG at room temperature (Supporting Information S1: Figure S5) reveal distinct peaks for each ingredient. Upon mixing, XRD reveals the emergence of broad shoulder peaks attributed to the pristine HC, alongside intricate diffraction peaks stemming from the ZG component. As the carbonization process (Figure 2A) proceeds, noticeable changes begin at 100°C, primarily due to the decomposition of ZG. At 200°C, significant decomposition of ZG takes place, resulting in the disappearance of characteristic peaks associated with the products, leaving behind amorphous characteristics. In this process, the molecules of ZG undergo degradation, leading to the volatilization of gas products and the generation of residual organic molecules. Upon reaching 400°C, the formation of zinc oxide crystal initiates, with their crystallinities and sizes continuing to increase above 600°C. As the temperature further increases, there is a slight catalysis of partial graphitization of the HC. Concurrently, a bulk-etching phenomenon is observed within the graphitic layers by the reaction $ZnO + C = Zn + CO\uparrow$, mostly producing metallic Zn, which can evaporate above 900°C [31]. Notably, this process results in the formation of plenty of small voids within HC, further impeding directed graphitization and generation of a large number of nanopores. However, as the carbon layer densifies, a minute portion of internal ZnO is reduced to form zinc monoatoms, which become embedded within the HC. This phenomenon is reflected in the subsequent characterization. HRTEM images (Supporting Information S1: Figure S6a,b) demonstrate that ZG/HC-200 displays a high degree of disorder, and as the temperature increases, ZnO begins to emerge at 400°C, with a small amount of ZnO lattice becoming visible (Figure 2B,C). The appearance of ZnO persists at 600°C (Figure 2D,E), where

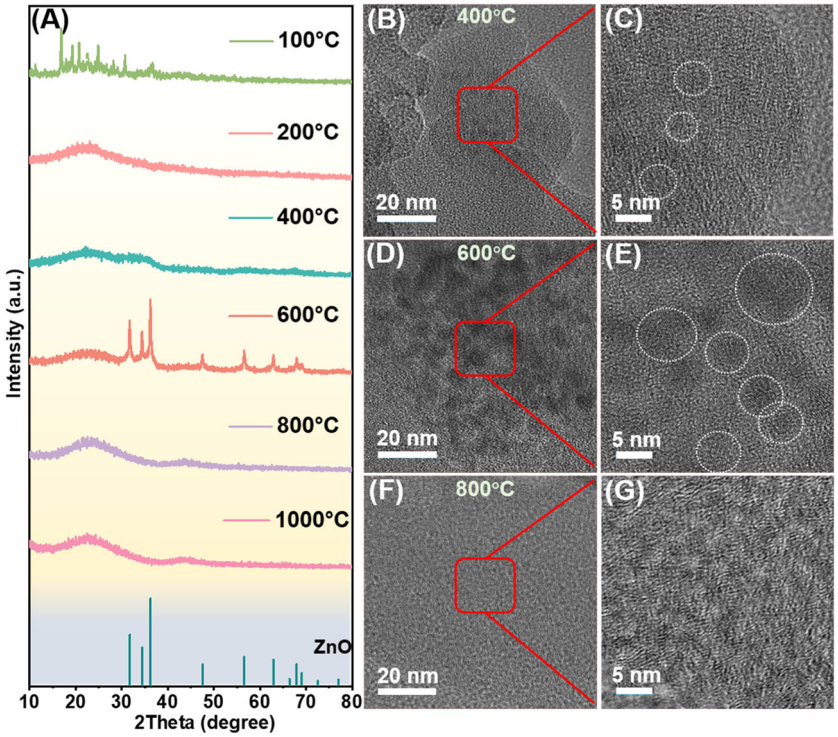

FIGURE 2 | (A) XRD patterns of composite samples treated at different temperatures. HRTEM images of composite samples treated at different temperatures (B, C) ZG/HC-400, (D, E) ZG/HC-600, and (F, G) ZG/HC-800.

metal lattice is scarcely observed and smaller nanopores begin to appear. At 800°C (Figure 2F,G), nanopores continue to grow, and the carbon layer becomes slightly more ordered. Further heating to 1000°C results in additional growth of nanopores, accompanied by a slight improvement in carbon layer orderliness (Supporting Information S1: Figure S6c,d). TEM results align well with XRD findings, illustrating that the formation of closed pores during ZG/HC pyrolysis involves the initial embedding of ZG into the carbon matrix, followed by the growth of ZnO to metallic Zn, which was then eliminated by high-temperature volatilization. The small amount of residual Zn within the HC contributes to the migration of sodium ions. The continuous development of graphite domains and shrinkage of partially open pores drive the transformation of open pores into closed pores.

In Figure 3A, the nitrogen adsorption–desorption isothermals for samples show a characteristic type IV adsorption curve, indicating a sharp pore size distribution that is concentrated primarily around 3.8 nm (Figure 3B), ideal for Na^+ ion diffusion. The pore numbers decrease with increasing temperature [32, 33]. The nitrogen adsorption–desorption measurements show sensitivity exclusively to the examination of external pore structures (those open, interconnected with the external environment), rendering them unsuitable for the analysis of internal pore structures (closed pores, enclosed areas within the material). During the process of carbonization at high temperatures, the formation of microcrystalline structures during a process can cause some external pore structures to transform into internal ones [34]. Figure 3C displays the microstructure of the samples obtained from small-angle X-ray scattering (SAXS) method. In the SAXS spectra, the medium region shows scattering from nanometer-sized structures, attributed to nanopores in HC. The lower Q region of the spectrum indicates scattering originating from larger-scale microstructural features, such as meso/macropores and particles. SAXS curves at ≈ 0.01-0.2 $Å^{-1}$ (Figure 3C inset) suggest an intensification of nanopore scattering as the charring temperature increases, suggesting the growth of closed nanopores. This phenomenon arises from the fusion of cellulose and other substances into a graphite-like layer, which contract in the presence of Zn to form closed pores [29]. The brightness of 2D SAXS images indicates a rich isotropic pore distribution, confirming diverse porosity (Figure 3D). The results of nanopore growth are consistent with the distribution of nanopore in HRTEM. The elemental makeup and states were investigated using X-ray photoelectron spectroscopy (XPS). The oxygen content of HC-1600 (3.53%) is significantly lower than that of HC-1200 (4.37%), indicating a loss of sp^3-hybridized carbon and C–O functional groups in the high-temperature carbonization process (Figure 3E, Supporting Information S1: Figure S7). The reduced oxygen content can minimize the initial capacity loss from irreversible Na^+ adsorption, enhancing the ICE and favoring practical electrode application [35, 36]. Additional, XPS results confirm the presence of Zn in the HC-1400 material. The elemental analysis by inductively coupled plasma mass spectrometry (ICP-MS) shows a Zn content of 0.005 wt% (Supporting Information S1: Table S1). The high-angle annular dark-field scanning transmission electron microscopy (HAADF-STEM) image displays a sparse, evenly distributed scattering of bright spots across the HC substrate (Figure 3F), revealing the atomic dispersion of Zn species. These trace zinc single atoms boost the ion transport rate [37].

To further elucidate the role of zinc single atoms, density functional theory (DFT) calculations are used to explore their

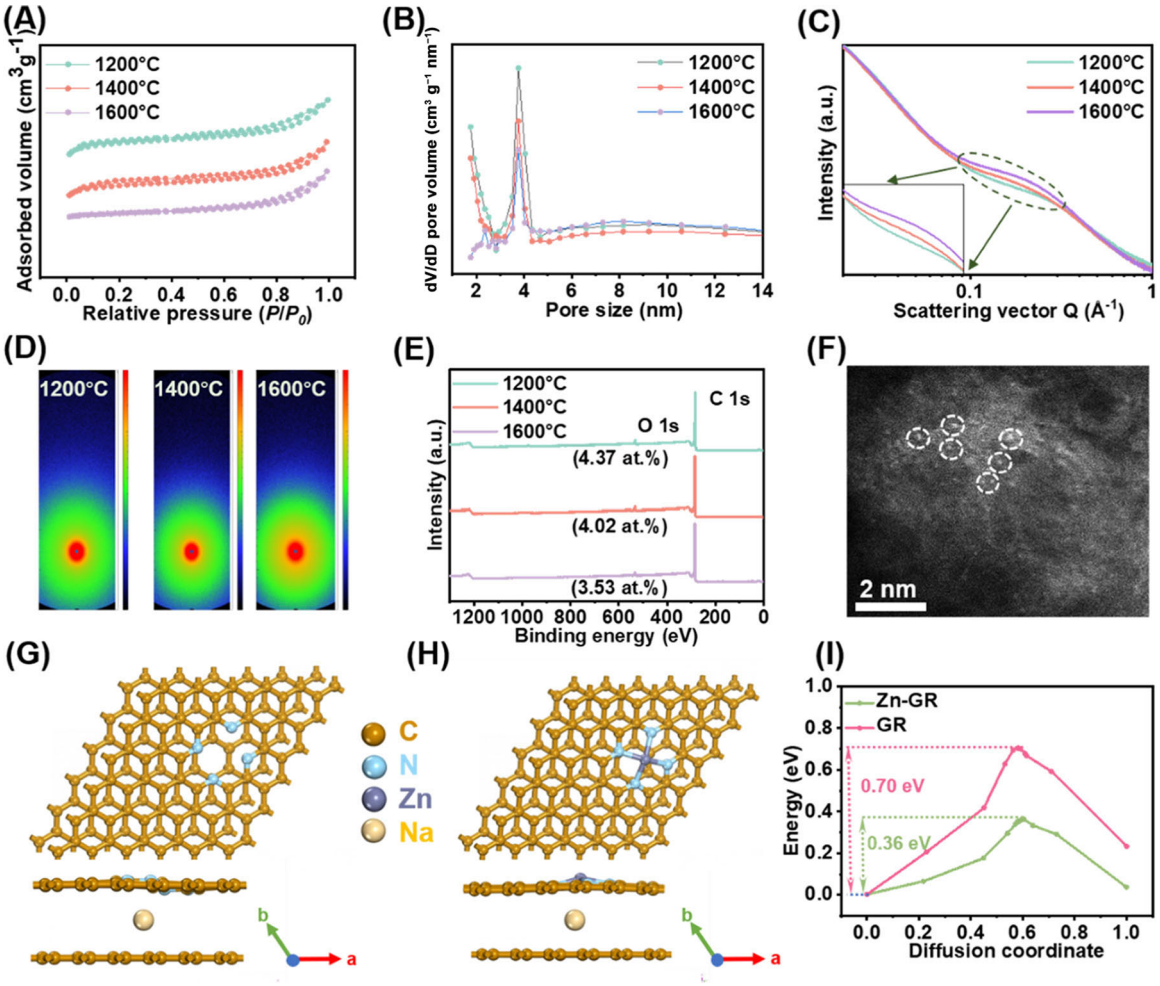

FIGURE 3 | (A) N_2 adsorption–desorption isotherms of HC-1200, HC-1400, and HC-1600. (B) Pore size distribution obtained from Barrett-Joyner-Halenda method. (C) Scattering vector Q (Å^{-1}). (D) 2D-SAXS images. (E) XPS spectra of HC-1200, HC-1400, and HC-1600. (F) HAADF-STEM image of HC-1400, showing the single atoms. Diffusion paths of Na^+ in (G) GR, and (H) Zn-GR. (I) Diffusion barrier energies of Na^+ in GR and Zn -GR.

impact on Na^+ storage kinetics. Two idealized models, graphite without metal atoms (GR) and graphite with zinc single atoms (Zn-GR), are constructed based on the microstructural features of HC. These models are used to simulate the Na^+ diffusion process within the graphite domains of Zn-HC and HC (Figure 3G,H). The adsorption sites and corresponding Na^+ adsorption energies are shown in Supporting Information S1: Figure S8, where GR shows a lower adsorption energy (−4.52 eV) compared to Zn-GR (−2.41 eV), suggesting that Zn single atoms do not serve as active sites for Na^+ adsorption. However, the calculated Na^+ diffusion energy barrier for Zn-GR (0.36 eV) is significantly lower, indicating that Zn single atoms promote Na^+ diffusion, which is a key factor contributing to the material's excellent rate capability (Figure 3I).

Building on these results, we carried out an in-depth exploration of the electrochemical characteristics of the materials utilized within a battery system. Charge/discharge curves of HC-1200, HC-1400, and HC-1600 half-cells show distinct regions at the slope and plateau region, indicating quintessential sodium-ion storage behavior observed in HC materials (Figure 4A and Supporting Information S1: Figure S9). The obvious potential plateau visible in the charge curve of HC-1400 at approximately 0.5 V is attributed to a redox reaction involving Na^+ and C═O [38, 39]. It is noteworthy that the sloping region associated with the C═O reduction reaction may be influenced by factors such as the C═O group and defects, potentially resulting in slopy charge/discharge behavior [40]. HC-1600, characterized by fewer defect counts and a decreased specific surface area, displays a notable high-voltage plateau. Conversely, HC-1200, with a higher defect content and lower degree of graphitization, displays an overall gradual charge/discharge curve [32, 34, 38, 41, 42]. Remarkably, HC-1400 delivers a much greater initial reversible capacity of 348.5 mAh g^{-1} at 30 mA g^{-1}, compared to HC-1200 (224.9 mAh g^{-1}) and HC-1600 (274.5 mAh g^{-1}). Additionally, it achieves an ICE of 92.84%. The HC without ZG displays a capacity of 291.0 mAh g^{-1}, with an ICE of 86.60% (Figure 4A). This enhancement is attributed to its ultra-small nanopores that selectively allow Na ion insertion while preventing electrolyte molecules from accessing the inner surface, thereby effectively avoiding excessive SEI film formation. Similar results are found in the cyclic voltammetry (CV) curve, which shows an irreversible redox peak in the first cycle, indicating electrolyte decomposition and the formation of an SEI film, accompanied by minimal side reactions (Figure 4C). The CV curve shows repetition in subsequent cycles and has a prominent redox peak pair within a low potential range. This observation

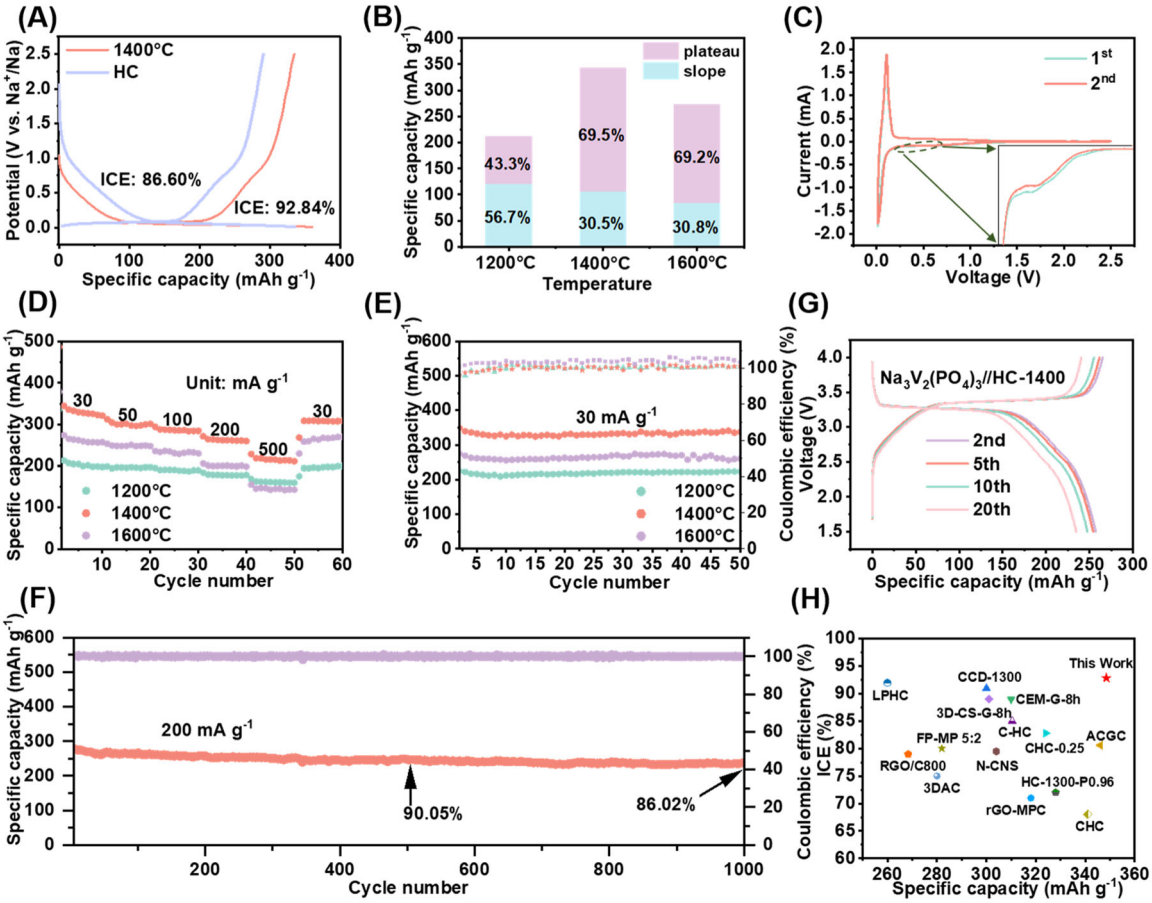

FIGURE 4 | (A) Comparison of the first discharge/charge curves for carbonized HC containing ZG at 1400°C and pure HC in half-cells. (B) Contribution ratios of the slope capacity and plateau capacity. (C) CV curves of HC-1400 at 0.2 mV s^{-1}. (D) Rate performances of HC-1200, HC-1400, and HC-1600 at current densities from 30 mA g^{-1} to 500 mA g^{-1}. (E, F) Cycling performance of HC-1200, HC-1400, and HC-1600 at current densities of 30 mA g^{-1} cycling performance of HC-1400 at current densities of 200 mA g^{-1}, respectively. (G) Second, fifth, tenth, and twentieth cycles of the full cell based on $Na_3V_2(PO_4)_3$//HC-1400. (H) Comparison of the ICE and specific capacity of representative HC anodes.

suggests that the storage of sodium ions within the carbon matrix has excellent reversibility (Supporting Information S1: Figure S10). More detailed analysis reveals that the plateau portion of HC-1400 (0.1–0.01 V) constitutes 69.50% of the total capacity, surpassing HC-1200 and closely aligning with HC-1600 (Figure 4B). Such a salient plateau capacity in HC-1400 can be attributed to its abundance of closed pores, recognized as superior Na^+ storage sites [23]. These findings emphasize the link between Na^+ storage capacity and a closed pore structure [22]. Furthermore, HC-1400 demonstrates outstanding rate capability, achieving an excellent capacity of 218.1 mAh g^{-1} at 500 mA g^{-1}, outperforming HC-1200 and HC-1600, which have capacities of 162.8 and 146.9 mAh g^{-1}, respectively (Figure 4D). Although the capacity reduction at high current densities is partly attributable to the sluggish kinetics of closed pores serving as Na^+ storage sites, the presence of zinc single atoms significantly enhances ion transport rates, thereby improving high current densities performance compared to other biomass-derived carbon materials. All samples demonstrate remarkable stability over multiple cycles. Particularly noteworthy is HC-1400, which maintains a capacity of 340.5 mAh g^{-1} after 50 cycles, even at a current density of 30 mA g^{-1} (Figure 4E). Furthermore, at higher current densities, HC-1400 demonstrates impressive performance, retaining 90.05% capacity after 500 cycles at 200 mA g^{-1} and 86.02% after 1000 cycles (Figure 4F). In addition, the properties of electrode materials obtained by mixing HC with different mass ratios of ZG are compared (HC:ZG = 1:0.5 or 1:2). Too little ZG results in a synthesized hard carbon material without a rich closed pore structure, while too much ZG results in a large amount of Zn volatilizing at high temperatures to produce an unclosed pore, leading to a low ICE. And the HC-1400 anode shows the best rate performance and long cycle Performance (Supporting Information S1: Figure S11). Comparative analysis with previous reports on biomass-derived carbon materials highlights the significantly higher reversible capacity and ICE of the as-prepared HC-1400 (Figure 4H) [38, 43–52]. In a practical application, HC-1400 serves as an anode paired with a $Na_3V(PO_4)_3$ cathode to construct a full cell. Also, this full cell demonstrates a high discharge capacity of 265.0 mAh g^{-1}. Additionally, it offers an output voltage of 3.2 V and maintains excellent capacity retention of 60.83% even after 100 cycles (Figure 4G and Supporting Information S1: Figure S12). These results highlight its significant potential for practical commercial applications.

In order to investigate the impact of microstructural modifications on the storage behavior of sodium ions, a kinetic study of HC-1400 was carried out using CV and the galvanostatic intermittent titration technique (GITT). The CV curves of

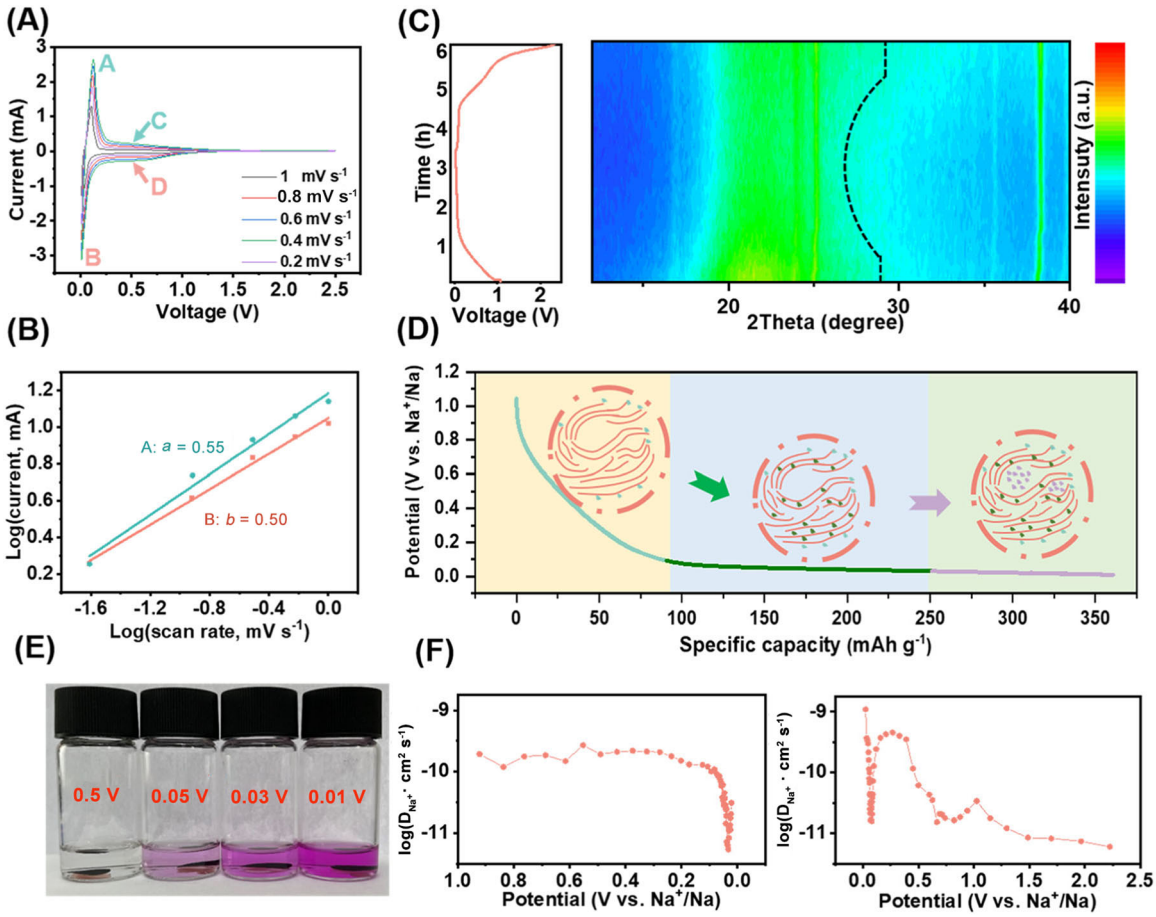

FIGURE 5 | (A) CV curves of HC-1400 at different scan rates. (B) *b*-Value fitting diagram of the CV peak of the HC-1400 electrode. (C) In situ XRD patterns and the corresponding Galvanostatic charge-discharge curve at 100 mA g^{-1}. (D) Schematic diagram of the sodium storage mechanism of HC. (E) Color changes of the HC-1400 electrode with ethanol at different potentials. (F) Sodium-ion diffusion coefficients from the sodiation and desodiation process estimated from GITT curves.

HC-1400 were recorded at various scan rates of 0.2 ~ 1 mV s^{-1} (Figure 5A). On the basis of the relationship between current and scan rate, the storage behavior of Na^+ can be calculated from the *b*-value using the following formulas:

$$i = av^b, \tag{1}$$

$$\log i = b \log v + \log a, \tag{2}$$

where *a* and *b* are the relevant parameters; *i* and *v* are the current and scanning rates, respectively. When the value of *b* approaches 1, it is shown that the storage mechanism of the material is controlled by capacitive contribution. Also, when the *b* value is 0.5, a diffusion-controlled process occurs in the HC anode [53, 54]. In Figure 5b, the calculated *b* value for the peak (HC-1400) approaches 0.5, which demonstrates the presence of a diffusion-controlled mechanism. In contrast, the *b* value is 1.0/0.92 for the peak at 0.5 V, which means that the slope region is determined by capacitive behavior (Supporting Information S1: Figure S13). Other materials show similar results (Supporting Information S1: Figure S14–S16). Moreover, the sodium-ion storage mechanisms of HC-1400 are also uncovered by in situ XRD measurement (Figure 5C) [55]. When discharged from the initial voltage to 0.1 V, the (002) peak of the sample was hardly displaced, demonstrating that Na^+ ions were predominantly adsorbed on the surface. After the voltage dropped below 0.1 V, significant shift of the (002) peaks toward the left confirms the insertion of Na^+ ions into the carbon layers (see the schematic illustration in Figure 5D). In the process of charging, the (002) peak of HC-1400 is retained in the same place, and when the cell is charged to 2.5 V, the (002) peak of HC-1400 returns to its original position. These data provide additional evidence that the suitable interlayer spacing of HC-1400 favors the reversible reactions of Na^+, thus contributing to outstanding cycling stability.

To gain a deeper insight into how HC-1400 stores sodium in the low-voltage plateau region, the HC electrodes discharged to 0.5 V, 0.05 V, 0.03 V and 0.01 V were disassembled and soaked in a solution of phenolphthalein/ethanol. And sodium quasi-metal reacts with ethanol to form H_2 and CH_3CH_2ONa. When the reaction occurs, it causes the phenolphthalein solution to turn red [23]. As the discharge process continues, the color of the ethanol solution gradually intensifies (Figure 5E). When discharged to 0.01 V, a large amount of H_2 gas is produced when the pole piece comes into contact with the solution, and the solution becomes darker in color, indicating the presence of quasi-metallic sodium in the nanopores of the HC-1400 material, which corresponds to the Na filling process. In addition, the electrode was analyzed using GITT with a pulse current of 30 mA g^{-1} (Supporting Information S1: Figure S17), and the

corresponding diffusion coefficients (D_{Na^+}) are presented in Figure 5F [38, 56]. Impressively, in the slope region, where the D_{Na^+} value stabilizes, a high level of Na^+ diffusivity is observed during the adsorption process that occurs on the surface of the carbon material. In the plateau region, D_{Na^+} values decrease and then increase; the sharp decline in D_{Na^+} values within the range of approximately 0.1 to 0.05 V is attributed to the intercalation of Na^+ through the carbon layer with the interior of HC-1400, whereas at 0.05 V, the diffusion coefficient shows an extremely rapid increase, which is attributed to the sodium ions starting to fill the nanopores. The findings suggest that sodium ions primarily undergo three processes: adsorption in the slope region, intercalation into the carbon layers, and subsequent reduction to form sodium clusters that fill the enclosed pores. In summary, the material follows an "adsorption–intercalation–pore filling" sodium storage mechanism.

3 | Conclusions

In summary, we have developed a HC material with low defects, abundant nanopores, and long-order curved graphite domains using a facile ZG-assisted catalytic process. The conversion of ZG into ZnO during preparation results in HC with expanded interlayer spacings, abundant turbostratic nanoregions, and closed pores. With an increase in temperature, a large amount of ZnO is reduced and volatilized at high temperatures. Additionally, trace amounts of single zinc atoms remain in the HC, significantly enhancing ion-transfer mobility. Our comprehensive investigation confirms the coexistence of interlayer Na^+ intercalation and nanopore Na filling in the low-voltage plateau region during cycling. This dual mechanism, driven by both optimal layer spacing and nanopores, underpins the excellent performance of the HC material. Consequently, the HC-1400 electrode achieves a capacity of 348.5 mAh g^{-1}, with an ICE of 92.84%, demonstrating its potential for use as a high-performance anode material for sodium-ion batteries.

Acknowledgments

Y. Z. acknowledges the support from the National Natural Science Foundation of China (22209103). H.G. and Y.W. acknowledge the support from the Open Project of State Key Laboratory of Advanced Special Steel, the Shanghai Key Laboratory of Advanced Ferrometallurgy, Shanghai University (SKLASS 2021-04), the Science and Technology Commission of Shanghai Municipality (22010500400) and "Shanghai Pujiang Program" (23PJ1402800), "Joint International Laboratory on Environmental and Energy Frontier Materials," and "Innovation Research Team of High-Level Local Universities in Shanghai" at Shanghai University.

Conflicts of Interest

The authors declare no conflicts of interest.

References

1. L. L. Lu, Y. Y. Lu, Z. X. Zhu, et al., "Extremely Fast-Charging Lithium Ion Battery Enabled by Dual-Gradient Structure Design," *Science Advances* 8, no. 17 (2022): 2375–2548.

2. W. Cai, C. Yan, Y. X. Yao, et al., "The Boundary of Lithium Plating in Graphite Electrode for Safe Lithium-Ion Batteries," *Angewandte Chemie International Edition* 60, no. 23 (2021): 13007–13012.

3. Q. Man, C. Wei, K. Tian, et al., "Molecular-Level Design of High Flash Point Solvents Enables High-Safety and Dual-Function Chemical Presodiation of Hard Carbon and Alloy Anodes for High-Performance Sodium-Ion Batteries," *Advanced Energy Materials* 14, no. 24 (2024): 2401016.

4. J. Li, L. Gao, F. Pan, et al, "Engineering Strategies for Suppressing the Shuttle Efect in Lithium–Sulfur Batteries," *Nano-Micro Lett* 16, no. 1 (2023): 12.

5. R. Shao, Z. Sun, L. Wang, et al., "Resolving the Origins of Superior Cycling Performance of Antimony Anode in Sodium-Ion Batteries: A Comparison With Lithium-Ion Batteries," *Angewandte Chemie International Edition* 63, no. 11 (2024): 1521–3773.

6. Y. S. Hu, Y. Li, et al, "Unlocking Sustainable Na-Ion Batteries Into Industry," *ACS Energy Letters* 6, no. 11 (2021): 4115–4117.

7. D. Saurel, B. Orayech, B. Xiao, D. Carriazo, X. Li, and T. Rojo, "From Charge Storage Mechanism to Performance: A Roadmap Toward High Specific Energy Sodium-Ion Batteries Through Carbon Anode Optimization," *Advanced Energy Materials* 8, no. 17 (2018): 1703268.

8. Y. Huang, X. Hu, Y. Li, et al., "Demystifying the Influence of Precursor Structure on S-Doped Hard Carbon Anode: Taking Glucose, Carbon Dots, and Carbon Fibers as Examples," *Advanced Functional Materials* 34, no. 40 (2024): 2403648.

9. Y. Xiao, J. Xiao, H. Zhao, et al., "Prussian Blue Analogues for Sodium-Ion Battery Cathodes: A Review of Mechanistic Insights, Current Challenges, and Future Pathways," *Small* 20, no. 35 (2024): 2401957.

10. Z. Sun, J. Pan, W. Chen, et al, "Electrochemical Processes and Reactions in Rechargeable Battery Materials Revealed Via In Situ Transmission Electron Microscopy," *Advanced Energy Materials* 14, no. 2 (2023): 2303165.

11. Z. Chen, X. Wu, Z. Sun, et al., "Enhanced Fast-Charging and Longevity in Sodium-Ion Batteries Through Nitrogen-Doped Carbon Frameworks Encasing Flower-Like Bismuth Microspheres," *Advanced Energy Materials* 14, no. 22 (2024): 2400132.

12. J. Liu, L. Huang, H. Wang, et al., "The Origin, Characterization, and Precise Design and Regulation of Diverse Hard Carbon Structures for Targeted Applications in Lithium-/Sodium-/Potassium-Ion Batteries," *Electrochemical Energy Reviews* 7, no. 34 (2024): 34.

13. J. Chen, G. Zhang, J. Xiao, et al., "A Stress Self-Adaptive Bimetallic Stellar Nanosphere for High-Energy Sodium-Ion Batteries," *Advanced Functional Materials* 34, no. 1 (2024): 202307959.

14. J. Xiao, X. Li, K. Tang, et al., "Recent Progress of Emerging Cathode Materials for Sodium Ion Batteries," *Materials Chemistry Frontiers* 5 (2021): 3735–3764.

15. T. Zhang, T. Zhang, F. Wang, and F. Ran, "High-Efficiently Doping Nitrogen in Kapok Fiber-Derived Hard Carbon Used as Anode Materials for Boosting Rate Performance of Sodium-Ion Batteries," *Journal of Energy Chemistry* 96 (2024): 472–482.

16. L. J. Xie, C. Tang, M.-X. Song, et al., "Molecular-Scale Controllable Conversion of Biopolymers Into Hard Carbons Towards Lithium and Sodium Ion Batteries: A Review," *Journal of Energy Chemistry* 72 (2022): 554–569.

17. N. Sun, Z. Guan, Y. Liu, et al., "Extended "Adsorption-Insertion" Model: A New Insight Into the Sodium Storage Mechanism of Hard Carbons," *Advanced Energy Materials* 9, no. 32 (2019): 1901351.

18. H. Gao, J. Li, F. Zhang, et al., "Revealing the Potential and Challenges of High-Entropy Layered Cathodes for Sodium-Based Energy Storage," *Advanced Energy Materials* 14, no. 20 (2024): 2304529.

19. X. Guo, H. Gao, S. Wang, et al., "MXene-Based Aerogel Anchored With Antimony Single Atoms and Quantum Dots for High-Performance Potassium-Ion Batteries," *Nano Letters* 22, no. 3 (2022): 1225–1232.

20. J. Zhao, X. X. He, W. H. Lai, et al., "Catalytic Defect-Repairing Using Manganese Ions for Hard Carbon Anode With High-Capacity and High-Initial-Coulombic-Efficiency in Sodium-Ion Batteries," *Advanced Energy Materials* 13, no. 18 (2023): 2300444.

21. F. Chen, Y. Di, Q. Su, et al., "Vanadium-Modified Hard Carbon Spheres With Sufficient Pseudographitic Domains As High-Performanceanodefor Sodium-Ion Batteries," *Carbon Energy* 5, no. 2 (2022): e191.

22. K. Wang, F. Sun, H. Wang, et al., "Altering Thermal Transformation Pathway to Create Closed Pores in Coal-Derived Hard Carbon and Boosting of Na^+ Plateau Storage for High-Performance Sodium-Ion Battery and Sodium-Ion Capacitor," *Advanced Functional Materials* 32, no. 34 (2022): 2203725.

23. Z. Zheng, S. Hu, W. Yin, et al., "CO_2-Etching Creates Abundant Closed Pores in Hard Carbon for High-Plateau-Capacity Sodium Storage," *Advanced Energy Materials* 14, no. 3 (2024): 2303064.

24. Y. Huang, X. Zhong, X. Hu, et al., "Rationally Designing Closed Pore Structure by Carbon Dots to Evoke Sodium Storage Sites of Hard Carbon in Low-Potential Region," *Advanced Functional Materials* 34, no. 4 (2024): 2308392.

25. C. Yu, Y. Li, H. Ren, et al., "Engineering Homotype Heterojunctions in Hard Carbon to Induce Stable Solid Electrolyte Interfaces for Sodium-Ion Batteries," *Carbon Energy* 5, no. 1 (2022): e220.

26. H. Chen, N. Sun, Q. Zhu, R. A. Soomro, and B. Xu, "Microcrystalline Hybridization Enhanced Coal-Based Carbon Anode for Advanced Sodium-Ion Batteries," *Advanced Science* 9, no. 20 (2022): 2200023.

27. M. Yuan, B. Cao, H. Liu, et al., "Sodium Storage Mechanism of Nongraphitic Carbons: A General Model and the Function of Accessible Closed Pores," *Chemistry of Materials* 34, no. 7 (2022): 3489–3500.

28. Z. Li, Y. Chen, Z. Jian, et al., "Defective Hard Carbon Anode for Na-Ion Batteries," *Chemistry of Materials* 30, no. 14 (2018): 4536–4542.

29. Z. Tang, R. Zhang, H. Wang, et al., "Revealing the Closed Pore Formation of Waste Wood-Derived Hard Carbon for Advanced Sodium-Ion Battery," *Nature Communications* 14 (2023): 6024.

30. Z. Song, M. Di, S. Chen, and Y. Bai, "Three-Dimensional N/O Co-Doped Hard Carbon Anode Enabled Superior Stabilities for Sodium-Ion Batteries," *Chemical Engineering Journal* 470 (2023): 144237.

31. X. Yin, Z. Lu, J. Wang, et al., "Enabling Fast Na^+ Transfer Kinetics in the Whole-Voltage-Region of Hard-Carbon Anodes for Ultrahigh-Rate Sodium Storage," *Advanced Materials* 34, no. 13 (2022): 2109282.

32. Y. M. Li, Y. S. Hu, M. M. Titirici, et al., "Hard Carbon Microtubes Made From Renewable Cotton As High-Performance Anode Material for Sodium-Ion Batteries," *Advanced Energy Materials* 6, no. 18 (2016): 1600659.

33. X. Yi, X. Li, J. Zhong, et al., "Unraveling the Mechanism of Different Kinetics Performance Between Ether and Carbonate Ester Electrolytes in Hard Carbon Electrode," *Advanced Functional Materials* 32, no. 48 (2022): 2209523.

34. F. Sun, H. Wang, Z. Qu, et al., "Carboxyl-Dominant Oxygen Rich Carbon for Improved Sodium Ion Storage: Synergistic Enhancement of Adsorption and Intercalation Mechanisms," *Advanced Energy Materials* 11, no. 1 (2021): 2002981.

35. M. Liu, J. Zhang, S. Guo, et al., "Chemically Presodiated Hard Carbon Anodes With Enhanced Initial Coulombic Efficiencies for High-Energy Sodium Ion Batteries," *ACS Applied Materials & Interfaces* 12, no. 15 (2020): 17620–17627.

36. D. Cheng, Z. Li, M. Zhang, Z. Duan, J. Wang, and C. Wang, "Engineering Ultrathin Carbon Layer on Porous Hard Carbon Boosts Sodium Storage With High Initial Coulombic Efficiency," *ACS Nano* 17, no. 19 (2023): 19063–19075.

37. Z. Lu, J. Wang, W. Feng, et al., "Zinc Single-Atom-Regulated Hard Carbons for High-Rate and Low-Temperature Sodium-Ion Batteries," *Advanced Materials* 35, no. 26 (2023): 2211461.

38. J. L. Xia, D. Yan, L. P. Guo, X. L. Dong, W. C. Li, and A. H. Lu, "Hard Carbon Nanosheets With Uniform Ultramicropores and Accessible Functional Groups Showing High Realistic Capacity and Superior Rate Performance for Sodium-Ion Storage," *Advanced Materials* 32, no. 21 (2020): 2000447.

39. X. Yin, Z. Lu, J. Wang, et al., "Enabling Fast Na Transfer Kinetics in the Whole-Voltage-Region of Hard-Carbon Anodes for Ultrahigh-Rate Sodium Storage," *Advanced Materials* 34, no. 13 (2022): 2109282.

40. Z. Hong, Y. Zhen, Y. Ruan, et al., "Rational Design and General Synthesis of S-Doped Hard Carbon With Tunable Doping Sites Toward Excellent Na-Ion Storage Performance," *Advanced Materials* 30, no. 29 (2018): 1802035.

41. H. Au, H. Alptekin, A. C. S. Jensen, et al., "A Revised Mechanistic Model for Sodium Insertion in Hard Carbons," *Energ Environ Sci* 14 (2020): 3216.

42. Y. Li, Y. Lu, Q. Meng, et al., "Regulating Pore Structure of Hierarchical Porous Waste Cork-Derived Hard Carbon Anode for Enhanced Na Storage Performance," *Advanced Energy Materials* 9, no. 48 (2019): 1902852.

43. D. Sun, B. Luo, H. Wang, Y. Tang, X. Ji, and L. Wang, "Engineering the Trap Effect of Residual Oxygen Atoms and Defects in Hard Carbon Anode Towards High Initial Coulombic Efficiency," *Nano Energy* 64 (2019): 103937.

44. F. Xie, Z. Xu, A. C. S. Jensen, et al., "Unveiling the Role of Hydrothermal Carbon Dots as Anodes in Sodium-Ion Batteries With Ultrahigh Initial Coulombic Efficiency," *Journal of Materials Chemistry A* 7 (2019): 27567–27575.

45. X. Zhao, Y. Ding, Q. Xu, X. Yu, Y. Liu, and H. Shen, "Low-Temperature Growth of Hard Carbon with Graphite Crystal for Sodium-Ion Storage With High Initial Coulombic Efficiency: A General Method," *Advanced Energy Materials* 9, no. 10 (2019): 1803648.

46. P. Lu, Y. Sun, H. Xiang, X. Liang, and Y. Yu, "3D Amorphous Carbon With Controlled Porous and Disordered Structures As a High-Rate Anode Material for Sodium-Ion Batteries," *Advanced Energy Materials* 8, no. 8 (2018): 1702434.

47. S. Yang, W. Dong, D. Shen, et al., "Composite of Nonexpansion Reduced Graphite Oxide and Carbon Derived From Pitch as Anodes of Na-Ion Batteries With High Coulombic Efficiency," *Chemical Engineering Journal* 309, no. 1 (2017): 674–681.

48. Z. Tang, S. Zhou, P. Wu, et al., "Engineering Surface Oxygenated Functionalities on Commercial Hard Carbon Toward Superior Sodium Storage," *Chemical Engineering Journal* 441, no. 1 (2022): 135899.

49. S. Guo, Y. Chen, L. Tong, et al., "Biomass Hard Carbon of High Initial Coulombic Efficiency for Sodium-Ion Batteries: Preparation and Application," *Electrochimica Acta* 410, no. 1 (2022): 140017.

50. B. Xiao, F. A. Soto, M. Gu, et al., "Lithium-Pretreated Hard Carbon As High-Performance Sodium-Ion Battery Anodes," *Advanced Energy Materials* 8, no. 24 (2018): 1801441.

51. J. Yang, X. Wang, W. Dai, et al., "From Micropores to Ultra-Micropores Inside Hard Carbon: Toward Enhanced Capacity in Room-/Low-Temperature Sodium-Ion Storage," *Nano-Micro Letters* 13, no. 98 (2021): 98.

52. Y. Zhao, Z. Hu, C. Fan, et al., "Novel Structural Design and Adsorption/Insertion Coordinating Quasi-Metallic Na Storage Mechanism Toward High-Performance Hard Carbon Anode Derived From Carboxymethyl Cellulose," *Small* 19, no. 41 (2023): 2303296.

53. S. Alvin, C. Chandra, and J. Kim, "Extended Plateau Capacity of Phosphorus-Doped Hard Carbon Used As an Anode in Na- and K-Ion Batteries," *Chemical Engineering Journal* 391, no. 1 (2020): 123576.

54. S. Qiu, L. Xiao, M. L. Sushko, et al., "Manipulating Adsorption-Insertion Mechanisms in Nanostructured Carbon Materials for High-Efficiency Sodium Ion Storage," *Advanced Energy Materials* 7, no. 17 (2017): 1700403.

55. Y. Li, Y. S. Hu, X. Qi, et al., "Advanced Sodium-Ion Batteries Using Superior Low Cost Pyrolyzed Anthracite Anode: Towards Practical Applications," *Energy Storage Materials* 5 (2016): 191–197.

56. Y. Chen, H. Sun, X. X. He, et al., "Pre-Oxidation Strategy Transforming Waste Foam to Hard Carbon Anodes for Boosting Sodium Storage Performance," *Small* 20, no. 12 (2024): 2307132.

Supporting Information

Additional supporting information can be found online in the Supporting Information section.